PAPER

Check for updates

Enhancing the reversibility of the chemical evolution of the Ni-rich LiNi$_{0.8}$Co$_{0.1}$Mn$_{0.1}$O$_2$ cathode *via* a simple pre-oxidation process†

Yan Mo,‡[ab] Shaofeng Liu,‡[ab] Guohui Yuan, ⬤ *[ab] Zikun Li,*[b] Meng Zhang[b] and Lingjun Guo*[c]

For developing commercially viable LiNi$_{1-x-y}$Mn$_x$Co$_y$O$_2$ (NCM), it is necessary to alleviate the irreversible chemical process upon Li-ion insertion/extraction, which primarily accounts for prevailing capacity loss, impedance buildup as well as low columbic efficiency. To resolve this issue, we herein propose a simple but novel method to alter the chemical composition by a facile treatment of H$_2$O$_2$, which remarkably reduces the cation mixing of Li$^+$/Ni^{2+} and residual lithium on the cathode. The tailored composition contributes great resistance to the structural reconstruction and enhancement in structural reversibility, as shown by *in situ* Raman and high-resolution transmission electron microscope (HRTEM) results. Thus, the modified sample outperforms the pristine one; it exhibits cyclability with 95.7% capacity retention over 300 cycles, high columbic efficiency and enhanced rate capability.

Introduction

Lithium-ion batteries (LIBs) occupy a favorable position in today's energy storage landscape: triumphing in the application of portable electronics in the early decades and now aiding their advancement in the fields of transportation and the grid storage market.[1,2] The cathodes are the limiting component but primary determinant for raising the power and energy density of LIBs.[3,4] In contrast to the conventional cathode material LiCoO$_2$, Ni-rich oxide cathodes (NCM), LiNi$_{1-x-y}$Co$_x$Mn$_y$O$_2$, have received widespread attention as potential high-performance cathode materials due to their high nickel fraction ($1 - x - y \geq 0.8$) boosting their practical capacity to above 200 mA h g^{-1}.[5] Structural and chemical instability induced by the progressive increment of Ni content, however, have hampered the application of NCM cathodes.[6–8] Notably, numerous studies have reported that the irreversible chemical evolution occurring in cathodes during the charge/discharge process can lead to failure in cycling stability, high voltage operation as well as reasonable columbic efficiency in the first few cycles. For instance, unstable structure instability induced by cation mixing and transition metal (TM) reduction, along with the phase transition from layered structure to spinel-like and $F\bar{3}m$, is related to the capacity fading and high-voltage failure.[9–11] Contaminating species that remain on the electrode surface caused by the synthesis procedure are another source of irreversible electrochemical process because they can react with electrolytes to generate excess side reaction.[12,13]

Surface amelioration and design are recognized as efficient remedies to solve these issues from chemical and structural degradation. Various surface coating, such as inert materials MgO, AlF, Li conductive materials (Li$_2$TiO$_3$ and LiCoO$_x$) and conductive polymer have been applied to the modification of the NCM materials.[14–19] Admittedly these efforts have contributed substantially to the cycle life and power performance, but most coating materials are isolated to the substrate material with obvious boundary, throwing barriers in the process of uniform distribution and complete protection for the NCM host upon prolonged cycling. Alternately, the pretreatment of cathode materials with mild acid (HNO$_3$, (NH$_4$)$_2$S$_2$O$_8$) or alkaline solution (N$_2$H$_4$) are demonstrated to be a facile strategy to alter the component of the material, which also displayed significant effect on the enhancement of the electrochemical behavior.[20–22] For example, it is widely reported that lithium depletion depth can be adjusted by using diluted HNO$_3$ solution based on the exchange between Li-ion and H-ion, which mitigated the initial capacity loss of the cathodes due to the leached Li$_2$O from the component.[21] Besides that, some researches confirmed that introducing oxidizing agents would be a good choice for enhancing the performance. Typically, KMnO$_4$ is widely reported to treat the precursor, in which a nanoscale thickness MnO$_2$ layer was induced into the outer and thus

[a]School of Chemistry and Chemical Engineering, Harbin Institute of Technology, Harbin 150001, People's Republic of China. E-mail: ygh@hit.edu.cn

[b]Shenzhen BTR Nanotechnology Co., Ltd, Shenzhen 518106, People's Republic of China. E-mail: lizikun@btrchina.com

[c]State Key Laboratory of Solidification Processing, Northwestern Polytechnical University, Xi'an 710072, China. E-mail: guolingjun@nwpu.edu.cn

† Electronic supplementary information (ESI) available. See DOI: https://doi.org/10.1039/d3ra07178b

‡ These authors contributed equally.

suppressed the capacity fade of the materials during cycling.[23] Han *et al.* reported Li-rich materials modified with $Na_2S_2O_8$, and found that crystal lattice O^{2-} was oxidized to O_2^{2-} and facilitated the chemical Li^+ de-intercalation.[24] Therefore, improvement mechanisms vary widely and depends on the properties of oxidizing agents. Compared to other oxidants, H_2O_2 can avoid introduction of heteroatoms of Na^+ or K^+ that may reduce the activity of NCM materials. However, H_2O_2 with strong oxidizing properties is less been reported on cathode material modification, and whether it contributes enhancement is still unclarified.

Motivated by the above study, we demonstrate a facile approach for concurrently enhancing the structural integrity and chemical composition of the Ni-rich $LiNi_{0.8}Co_{0.1}Mn_{0.1}O_2$ material, which aims to assist the electrochemical behavior in the Li-ion batteries. The preparation strategy of the modified $LiNi_{0.8}Co_{0.1}Mn_{0.1}O_2$ material is that a certain amount of H_2O_2 is adopted to treat the precursor of spherical $Ni_{0.8}Co_{0.1}Mn_{0.1}(OH)_2$, which leads to the oxidation of transition metal (TM) ions in varying degrees from the surface to outerlayer. Such pre-activation of the precursor provides decreased amount of Ni^{2+}, which is expected to mitigate the amount of lithium-deficient $Li_{1-x}Ni_{1+x}O_2$ during the following lithiation process, which specifically decreases the structural disordering and lithium residues remained on the particle surface of the final $LiNi_{0.8}Co_{0.1}Mn_{0.1}O_2$ products.

Experimental

Materials preparation

The hydroxide precursor $(Ni_{0.8}Co_{0.1}Mn_{0.1}(OH)_2)$ used here was synthesized by the co-precipitation method, the detailed process was presented in our previous report.[25] The pristine $LiNi_{0.8}Co_{0.1}Mn_{0.1}O_2$ denoted as N-NCM was produced by sintering the mixture of the precursor and LiOH powder with atomic ratio of Li/(Ni + Co + Mn) = 1.05 at 750 °C for 12 h under an O_2 flow. The modified material treated with different amounts of H_2O_2 here are denoted as H-1, H-2 and H-3. To synthesized the modified samples, the obtained precursors (1 g) were soaked in hydrogen peroxide (H_2O_2, 30 mL) solution and stirred for 20 min at room temperature, the H_2O_2 concentration is 5 mol L^{-1} for H-1, 10 mol L^{-1} for H-2, 15 mol L^{-1} for H-3. Then, the obtained substances were filtered to obtain the modified precursor and dried at 60 °C overnight. The modified precursors are calcining by using the same condition of N-NCM as mentioned above to produce the final H-1, H-2 and H-3 materials.

Materials characterization

The crystalline phase of the materials was characterized by the X-ray diffractograms (XRD) of Bruker D2 ADVANCE. The morphologies of the N-NCM and H-1, H-2 and H-3 materials were checked *via* scanning electron microscopy (SEM, FEI Helios Nanolab 600i). High-resolution morphological images were collected *via* the transmission electron microscope (TEM) with the equipment of Tecnai G2 F30 operated at 200 keV. The

surface configuration of the cycled cathodes is characterized by the X-ray photoelectron spectroscopy (XPS, Thermo ESCALAB 250). Raman spectroscopy is performed in the wavenumber range of 200–850 cm^{-1} by utilizing DXRxi from Thermo Fisher with a solid state laser source with 532 nm. The chemical composition was analyzed using an inductively coupled plasmas spectrometer (ICP, SPS-7800, Japan).

The cathode slurry was synthesized by mixing 80 wt% of active material, 10 wt% of conductive agent (Ketjenblack) dried under vacuum at 110 °C for 12 h and 10 wt% of poly-vinylidenedifluoride (PVdF) dissolved in *N*-methyl-2-pyrrolidone (NMP). Following, the resulting slurry was deposited on the aluminum foil and dried at 110 °C overnight. The foil was then cut into disk cathodes with 10 mm in diameter.

The electrodes were fabricated by adopting coin-typed cells (CR2025) in glove box from Mikrouna filled with argon gas. Lithium metal with a diameter of 10 mm pressed on the current collector was used as the counter electrode. A solution of 1 M $LiPF_6$ as electrolyte in EC and DMC was used in combination with PP separator (Celgard 2500). The battery for *in situ*-Raman measurements was a tailor-made coin cell, whose positive side of the cell case had a hole of 5 mm and the hole was covered by a window made by quartz.

Cyclic voltammetry (CV) and electrochemical impedance spectroscopy (EIS) were conducted on a multichannel workstation from Biologic VSP-300. The tests for CV used a scan rate of 0.05 to 1 mV s^{-1} between 2.7 and 4.5 V, for EIS were performed on a charged state of 4.5 V and used a frequency ranged from 100 kHz to 100 mHz. Galvanostatic cycling tests were carried out on the Landt cycler (series CT2001A) and a nominal current density of 1C (200 mA g^{-1}) was adopted for all cathodes to ensure the comparability. The differential capacity *vs.* voltage (dQ/dV) and the galvanostatic intermittent titration technique (GITT) were measured using HOKUTO DENKO test system.

Results and discussion

Despite the treatment with the strong oxidizing H_2O_2 solution, it is difficult to find differences in surface morphology (Fig. S1†) and chemical composition (Table S1†) among the pristine and the H_2O_2 treated samples. However, detailed divergences of the crystal structure are successfully detected by the XRD and Rietveld refinement (Fig. 1). The main diffractions for all materials are demonstrated to be a single phase, corresponded
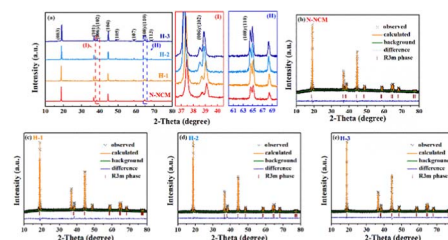

Fig. 1 XRD patterns (a) with the enlarged view of (006)/(102) (I) and (108)/(110) (II) splitting and the corresponded Rietveld refinements (b–e).

to LiNiO$_2$ (PDF 12-0543) in the hexagonal $R\bar{3}m$ space group.[26,27] With careful illustration of refinement results in Table 1, all modified materials exhibit obvious increase in lattice parameter c compared with the pristine sample. And more importantly, the percentage of Ni in Li layer (R(Ni/Li)) is restrained after H$_2$O$_2$ treatment, the R(Ni/Li) of H-3 sample and N-NCM sample is 5.86% and 0.28%, respectively, which can be also confirmed by the higher ratio of (003)/(104) peak for the H-2 (1.74) and H-3 material (1.76). The low Li/Ni mixing can be ascribed to the pre-oxidation process that significantly decreases the amounts of Ni^{2+} (Fig. S3†), in which the XPS signal of Ni^{3+} (857.6 eV) of the N-NCM precursor is barely invisible, while the proportion of Ni^{2+} to Ni^{3+} significantly decreases after H$_2$O$_2$ treatment. Meanwhile, upon close inspection, the enhanced crystallization of the enhanced crystallization of the modified materials can be further reflected by the two pairs of (006)/(102) and (108)/(110) splitting of the treated materials, which separates more obviously when compared with the patterns of N-NCM material (insert view of I and II in Fig. 1a).[28] Consequently, based on the above-mentioned results, it suggests that the peroxidation method promotes the structural ordering as well as the Li-ion diffusivity. Such improved structural properties of the modified materials are expected to show advantage in the following electrochemical performance.

Fig. 2 displays the charge and discharge profiles and corresponding dQ/dV curves of the first cycles for the NCM material treated with different amounts of H$_2$O$_2$. The N-NCM cathode has a more extended and lower platform during the initial charging process as compared with H-2 and H-3 cathodes, which is also can be reflected by the higher intensity of the peak for H1 phase in the dQ/dV (Fig. 2b). This suggests that the existence of contaminating species that remain on the electrode surface directly results spontaneous side reaction and lower columbic efficiency (83%).[28] But this phenomenon seems to be constrained after H$_2$O$_2$ treatment. The cathodes with H-2 and H-3 samples have a higher platform and H-2 sample shows the highest reversible capacity with a high columbic efficiency of 87%. To evaluate the cycling stability, the cathodes are examined at 1C first. As shown in Fig. 2c, the discharge capacity of the electrode with N-NCM sample reaches its pinnacle capacity of 183.7 mA h g^{-1} until 22 cycles and exhibits relatively low columbic efficiency around 95% at the first 30 cycles. Considering that the slowly growing capacity in the early cycles is resulted from the common effects of the lithium residues that remain on the surface, surface reconstruction and phase transition induced by cation migration, which cause a higher
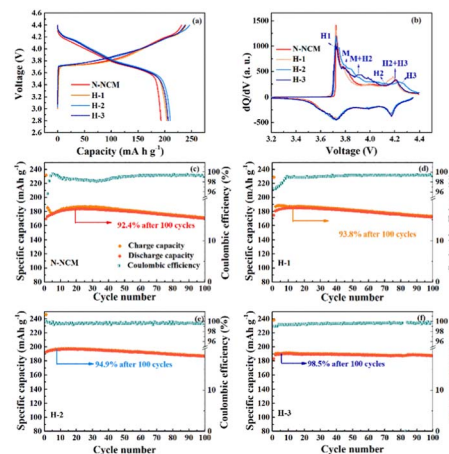

Fig. 2 The initial charge–discharge profile and corresponding dQ/dV results (a and b); the cycling performance at 1C (d–f).

activation energy barrier for Li-ion diffusion.[29–31] And obviously, such slow activation process also has a detrimental effect on the subsequent cycling and causes less stability of N-NCM cathode with capacity retention of 92.4% detected within 100 cycles. But it seems that the irreversible capacity in the early cycles can be mitigated in the modified materials by increasing the amount of H$_2$O$_2$. It can be seen in Fig. 2d–f, the capacity of modified materials is higher and reaches their pinnacle earlier as compared with the pristine, 185.2 mA h g^{-1} for H-1 sample at 15th cycle, 196.3 mA h g^{-1} for H-2 sample at 11th cycle and 190.1 mA h g^{-1} at 9th cycle for H-3 sample. And all of these modified materials show improved columbic efficiency and conserve their capacity better to that of the pristine one. Most notably, the H-2 and H-3 samples exhibit superior capacity retention of 94.9% and 98.5% after 100 cycles, respectively.

Fig. 3a compares the long-term cycling performance for all materials at a high rate of 5C. As seen, the electrode with N-NCM material delivers a pinnacle 147.3 mA h g^{-1} with capacity retention of 76.7% after 300 cycles. In contrast to the drastic capacity fading of N-NCM sample, all the modified samples outperform the pristine one in capacity retention after 300 cycles, 88.9% for H-1, 95.7% for H-2 and 95.0% for H-3. Meanwhile, as illustrated in Fig. S2,† the central voltage plateau of the N-NCM sample decreases to below 3.3 V after 300 cycles, while that of the H-2 and H-3 sample varies from the initial 3.75 V to 3.63 V, 3.60 V, respectively, after 300 cycles. The rate capability at 0.5C–10C also demonstrates the superiority of

Table 1 Results of XRD Rietveld refinements

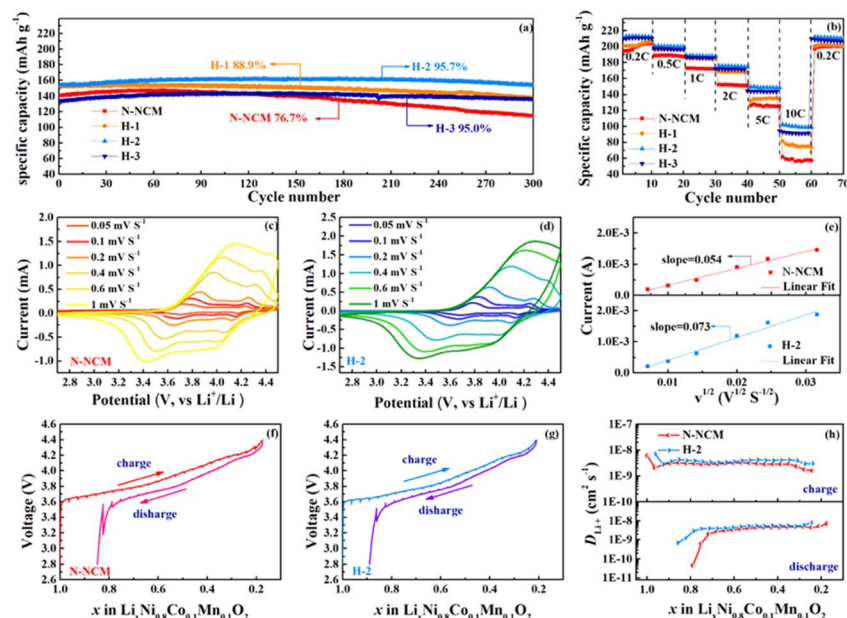|	Lattice parameters					R(Ni/Li) (%)	R_{wp} (%)
Sample	a (Å)	c (Å)	V (Å^3)	c/a	I(003)/I(106)		
N-NCM	2.879358	14.24321	102.266	4.946	1.62	5.86	2.81
H-1	2.879287	14.24393	102.267	4.947	1.60	4.76	2.37
H-2	2.881170	14.26756	102.569	4.952	1.74	0.34	2.08
H-3	2.879441	14.24634	102.294	4.948	1.76	0.28	2.16

Fig. 3 The cycle life at 5C (a) and rate capability (b) in the voltage range of 2.8–4.4 V; CV curves scan at different rates (c and d) and the oxidative peak current as a function of $v^{1/2}$ (e); GITT plots of the second cycle (f and g) and the calculated D_{Li^+} (h).

H_2O_2-treated samples (Fig. 3b). Although the differences between their capacities below 0.5C are negligible, the modified materials maintain much higher capacity than that of pristine during the subsequent cycles. With H_2O_2 amounts increasing, the relative high capacity 148.6 mA h g^{-1} for H-2 sample and 143.19 mA h g^{-1} for H-3 sample at 5C, and 101.0 mA h g^{-1} for H-2 sample and 91.8 mA h g^{-1} for H-3 sample at 10C are detected. The cation mixing of the materials can affect dynamic characteristic of N-NCM as well, which is responsible for opened Li-ion mobility channel during cycling. Therefore, the H-2 and H-3 samples with better structural integrity have much enhanced cycling stability and rate capability.

CV and GITT are used to evaluate the diffusion coefficient of Li-ions (D_{Li^+}), which reflect the electrochemical kinetic properties (Fig. 3c–h). Based on the CV experiment, the D_{Li^+} of N-NCM and H-2 samples are to be 7.44×10^{-10} cm^2 s^{-1} and 1.36×10^{-9} cm^2 s^{-1}, respectively, according to the Randle–Sevcik equation.[32] This superiority is also demonstrated by GITT, in which the detailed D_{Li^+} of the N-NCM and H-2 samples during the entire charge/discharge process is presented in Fig. 3h. The measured D_{Li^+} ranges from 4.5×10^{-11} cm^2 s^{-1} and 7×10^{-9} cm^2 s^{-1} along with the increased value of the modified cathode, which is consistent with the results from CV. Additionally, the extremely low D_{Li^+} of N-NCM cathode (4.52×10^{-11} cm^2 s^{-1}) appearing at the end of discharge accounts for the capacity fading upon a cycle.[33] Comparably, the D_{Li^+} of H-2 sample is 6.77×10^{-10} cm^2 s^{-1} at the end of discharge, much larger than that of the N-NCM cathode, indicating the improved chemical reversibility on the modified material once more.

In situ Raman spectroscopy is carried out to better understand the contribution of the hierarchical composition on the electrochemical response and related structure changes during cycling. Corresponding counter map and detailed position and

intensity change of E_g in the first two cycles of the N-NCM and H-2 samples are compared in Fig. 4. Upon charging, the $A1_g$ peak apparently declined to a minor signal is assigned to the generation of Li-ion vacancy[30]. But it is difficult to track and fit it because of its low intensity. As for E_g peak, the intensity for the H-2 sample exhibits a monotonically increase as the potential increases, which originates from the gradually oxidized nickel ion.[31] By contrast to the H-2 sample, there is a segment of abruptly week intensity for the N-NCM sample during the delithiation progress ($0.7 < x < 0.3$), which indicates the appearance of excess side reaction resulted from the surface contaminating species as well as the cation mixing. This
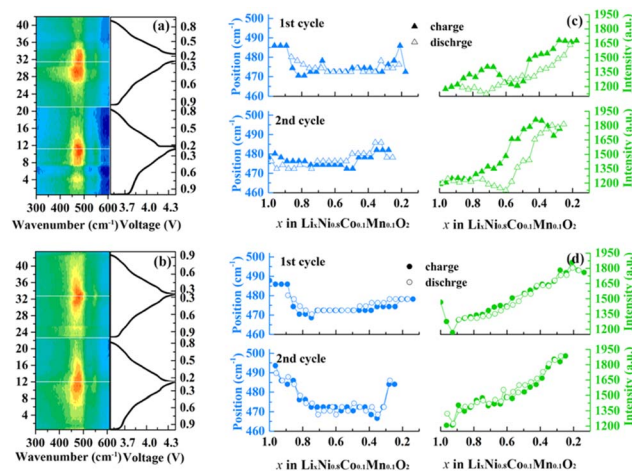

Fig. 4 *In situ* Raman during the first two cycles at 0.1C: the contour plot of the N-NCM (a) and H-2 (b) samples; band intensities and position of the E_g band of N-NCM (c) and H-2 (d) samples as a function of x.

discrepancy between the two samples would in turn confirm that the pre-oxidation procedure can effectively prevent surface reconstruction and undesired structural transition. Additionally, the band shift during cycling is also a significant parameter to determine the structure and symmetry, which is related to the variation of lattice parameters and coordination within the TMO_6 unit.[30] In the case of H-2 sample, the band position of E_g ($p(E_g)$) exhibits a U-shape trend, which decreases first to lower wavenumber and maintains a constant upon $0.4 < x < 0.8$, hereafter the $p(E_g)$ again increases. Unlike the case of H-2, where both the $p(E_g)$ and $I(E_g)$ well overlap during charge and discharge of the initial two cycles, charging the N-NCM cathode to 4.4 V leads to a hysteresis in $p(E_g)$ and $I(E_g)$, which confirms that the tailored composition of H-2 sample is favorable for maintaining the structural reversibility upon cycling.

To further detect the structural stability, the cycled cathodes for the N-NCM and H-2 samples are detected by HRTEM (Fig. 5). Apparently, we can find large areas of NiO rock-salt on the surface of the N-NCM particles but find a few for the H-2 particles after long-term cycling. In the case of the particle of N-NCM, its surface mainly contains group with layered $R\bar{3}m$ structure after 10th cycle but some dominant of mixed phases with NiO-like impurities (Fig. 5a). After 100 cycles, the NiO-like impurities with a thickness above 15 nm are observed in the surface of the N-NCM particle, which can be confirmed by the fast Fourier transform (FFT) pattern exhibited $Fm\bar{3}m$ structure (Fig. 5c). These impurities lead to ironically inert layer from continuous cation mixing during repeated cycling, which is also responsible for the increment of impendence and thus the capacity fading. By contrast, the H-2 electrode after 10th cycle shows a bulk of layered structure with $R\bar{3}m$ phase and a thin surface layer of $Fm\bar{3}m$ phase (Fig. 5b). After 100 cycles, inherently generated layer with mixed phases is also observed in the particle surface of H-2 electrode, but its thickness is well retained at about 5 nm (Fig. 5d). This observation further confirms that the H_2O_2 pretreatment is helpful for suppressing the structural distortion and leading to more sustainable intercalation reaction.

The depth XPS conducted around 40 nm from the top surface further gives an insight to the considerable improvement in the electrochemical performance (Fig. 6). As shown in Fig. 6a and c, the C 1s spectra can be fitted into four peaks, C=O, C–O, PVdF and C–C, respectively located at binding energies
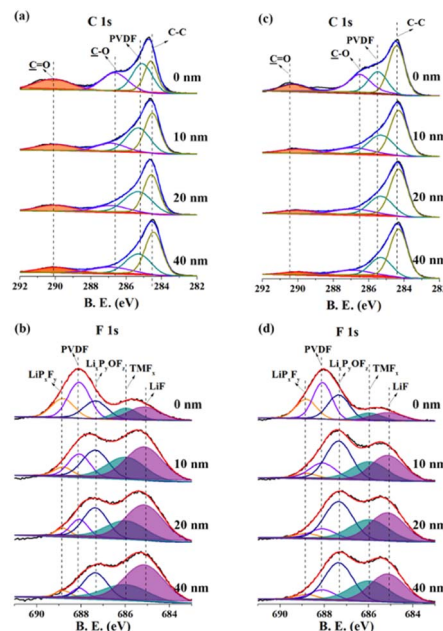

Fig. 6 Depth XPS of the charged electrodes for the (a and b) N-NCM and (c and d) H-2 samples after 100th cycle at 1C.

of 290.45 eV, 286.45 eV, 285.51 eV and 284.39 eV.[33] In the case of N-NCM, the C=O assigned to the Li_2CO_3 is relatively high, suggesting a high quantity of residual lithium species that inhibits the migration of Li-ions and electrons[33]. But the peak intensity for C=O in the case of NCM622 sample shows sharp reduction from 0 nm to 40 nm, indicating that the pre-oxidation process improve the utilization of lithium source and thus facilitates the Li-ion storage process. Besides, observed peaks in the F 1s spectra are associated with electrolyte decomposition products (LiP_xF_y, 688.86 eV; $Li_xP_yOF_z$, 687.28 eV; TMF_x, 685.94 eV; LiF, 685.06 eV) as well as PVdF binder (688.10 eV).[28] LiF and TMF_x is the result of the substrates dissolution of NCM cathode, therefore the relative intensity of gradually increases from inside out. The LiP_xF_y and $Li_xP_yOF_z$ are the byproducts of electrolyte decomposition, thus their intensity gradually decreases from inside out. Notably, the peaks for the parasitic-reaction products of LiF and TMF_x are fairly pronounce in the case of N-NCM, especially in the depth up to 20 nm, where the total quantity of LiF and TMF_x accounts for a much larger proportion than the other species (Fig. 6b). By contrast, the amounts ratio of LiF and TMF_x of the H-2 sample are significantly reduced. Even at the depth of the 40 nm, the surface of the H-2 electrode mostly consists of $Li_xP_yOF_z$ rather than that of LiF or TMF_x (Fig. 6d). Such reduced parasitic reaction products clearly confirms that the pre-oxidation method is also conducive to the stability of the electrode/electrolyte interface.

As illustrated above, our designed H-2 material with unique architecture, showing enhanced Li-ion mobility and reversibility during repeated Li-ion insertion/extraction, makes it possible to achieve 95.7% capacity retention over 300 cycles when cycling at 4.4 V. The kinetics of the electrodes during cycling is further examined by EIS. It can be seen in Fig. 7, all plots exhibit a semicircle lied in the high-to medium frequency
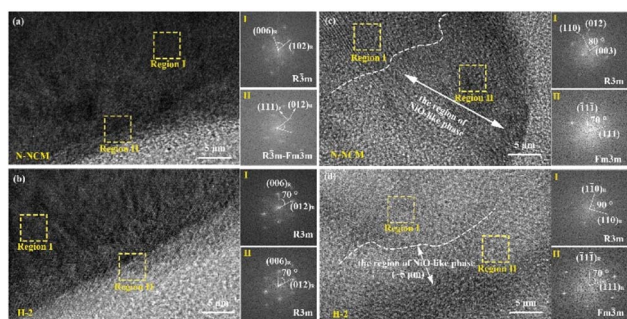

Fig. 5 HRTEM images of the charged electrodes after 10th (a and b) and 100th (c and d) cycle at the rate of 1C.
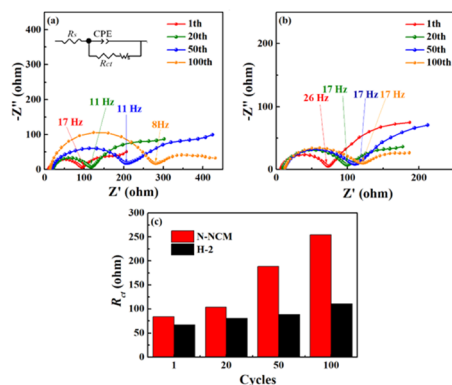
Fig. 7 Nyquist plots for the (a) N-NCM and (b) H-2 cells charged to 4.4 V at 1C; (c) R_{ct} calculated by the equivalent circuit drawn in (a).

and attributed to the resistances of charge transfers (R_{ct}) on the electrodes. As the cycling proceeded, R_{ct} of the pristine cell increases considerably as compared with that of the H-2 cell. The increment in R_{ct} for the pristine is almost three times its initial value, which can be ascribed to the gradually generated byproducts that are highly resistant to the diffusion of both Li-ions and electronics. By contrast, the R_{ct} of H-2 cell increases more slowly, showing 66.6 Ω at 1st and 90 Ω at 110.6th, indicating that adverse side reaction occur less extensively for the H-2 cell, which is also consistent with the result of the XPS.

Conclusions

In summary, a facile approach for unique architecture construction is proposed to enhance the chemical reversibility of Ni-rich-layered cathode *via* the treatment of H_2O_2. The modified materials show significantly reduced Li^+/Ni^{2+} mixing to below 0.34%, which is attributed to the H_2O_2 preoxidation that increases the amount of Ni^{3+} and mitigates the lithium-deficient $Li_{1-x}Ni_{1+x}O_2$. This is also proved by the domains enriched with Ni^{3+} detected by Raman mapping. The electrochemical properties of the modified one show extended capacity retention of 98.5% over 100 cycles, better rate capability as well as higher columbic efficiency when working up to 4.4 V. To elucidate the superiority of the modified material on the structure integrity, the examination of *in situ* Raman within the first two cycles and HRTEM obtained after cycling are conducted. As compared with the N-NCM, the peak intensity and position of the E_g mode for the modified one is more reversible upon charge/discharge and the amount of NiO-like phase is effectively restrained during cycling. Furthermore, the depth XPS suggests that the residual lithium remain on the electrode surface as well as the side reaction products (TMF_x and LiF) are significantly reduced after H_2O_2 modification, further proving the outstanding functionality of the modification.

Author contributions

Yan Mo and Shaofeng Liu conceived the idea, synthesized materials and wrote the original draft. ZiKun Li: and Meng

Zhang carried out the electrochemical measurements and data analysis. Lingjun Guo conducted the *in situ* Raman test and data analysis. Guohui Yuan charged with financing, reviewed and edited the manuscript.

Conflicts of interest

The authors declare no conflict of interest.

Notes and references

1 M. S. Whittingham, *Chem. Rev.*, 2004, **104**, 4271.
2 V. Etacheri, R. Marom, E. Ran, G. Salitra and D. Aurbach, *Energy Environ. Sci.*, 2011, **4**, 3243–3262.
3 J. Li, M. Zhang, D. Zhang, Y. Yan and Z. Li, *Chem. Eng. J.*, 2020, **402**, 126195.
4 J. Kim, H. Cho, H. Y. Jeong, H. Ma, J. Lee, J. Hwang, M. Park and J. Cho, *Adv. Energy Mater.*, 2017, **7**, 1602259.
5 S. S. Zhang, *Energy Storage Mater.*, 2020, **24**, 247–254.
6 D. Liu, S. Liu, C. Zhang, L. You, T. Huang and A. Yu, *ACS Sustainable Chem. Eng.*, 2019, **7**, 10661–10669.
7 J. H. Kim, S. J. Kim, T. Yuk, J. Kim, C. S. Yoon and Y. K. Sun, *ACS Energy Lett.*, 2018, **3**, 3002–3007.
8 F. Zhao, X. Li, Y. Yan, M. Su, L. Liang, P. Nie, L. Hou, L. Chang and C. Yuan, *J. Power Sources*, 2022, **524**, 231035.
9 F. Lin, I. M. Markus, D. Nordlund, T. C. Weng, M. D. Asta, H. L. Xin and M. M. Doeff, *Nat. Commun.*, 2014, **5**, 3529.
10 C. Xu, W. Xiang, Z. Wu, L. Qiu, Y. Ming, W. Yang, L. Yue, J. Zhang, B. Zhong, X. Guo, G. Wang and Y. Liu, *Chem. Eng. J.*, 2021, **403**, 126314.
11 F. Wu, J. Tian, N. Liu, Y. Lu, Y. Su, J. Wang, R. Chen, X. Ma, L. Bao and S. Chen, *Energy Storage Mater.*, 2017, **8**, 134–140.
12 K. Min, C. Jung, D. S. Ko, K. Kim, J. Jang, K. Park and E. Cho, *ACS Appl. Mater. Interfaces*, 2018, **10**, 20599–20610.
13 W. Li, H. Y. Asl, Q. Xie and A. Manthiram, *J. Am. Chem. Soc.*, 2019, **141**, 5097–5101.
14 H. Deng, P. Nie, H. Luo, Y. Zhang, J. Wang and X. Zhang, *J. Mater. Chem. A*, 2014, **2**, 18256–18262.
15 W. S. Yoon, K. W. Nam, D. Jang, K. Y. Chung, J. Hanson, J. M. Chen and X. Q. Yang, *J. Power Sources*, 2012, **217**, 128–134.
16 S. H. Ju, I. S. Kang, Y. S. Lee, W. K. Shin, S. Kim, K. Shin and D. W. Kim, *ACS Appl. Mater. Interfaces*, 2014, **6**, 2546–2552.
17 J. Liu and A. Manthiram, *Chem. Mater.*, 2009, **21**, 1695–1707.
18 H. Kim, M. G. Kim, H. Y. Jeong, H. Nam and J. Cho, *Nano Lett.*, 2015, **15**, 2111–2119.
19 W. Zhang, L. Liang, F. Zhao, Y. Liu, L. Hou and C. Yuan, *Electrochim. Acta*, 2020, **340**, 135871.
20 C. Yang, Q. Zhang, W. Ding, J. Zang, M. Lei, M. Zheng and Q. Dong, *J. Mater. Chem. A*, 2015, **3**, 7554–7559.

© 2024 The Author(s). Published by the Royal Society of Chemistry

21 S. H. Kang, C. S. Johnson, J. T. Vaughey, K. Amine and M. M. Thackeray, *J. Electrochem. Soc.*, 2006, **153**, A1186.

22 P. Oh, S. Myeong, W. Cho, M. J. Lee, M. Ko, H. Y. Jeong and J. Cho, *Nano Lett.*, 2014, **14**, 5965.

23 B. Huang, M. Wang, X. Yang, G. Xu and Y. Gu, *J. Alloys Compd.*, 2019, **808**, 151683.

24 S. Han, B. Qiu, Z. Wei, Y. Xia and Z. Liu, *J. Power Sources*, 2014, **268**, 683–691.

25 Y. Mo, L. Guo, B. Du, H. Jin, B. Cao, Y. Lu, D. Li and Y. Chen, *J. Power Sources*, 2020, **477**, 228699.

26 T. Ohzuku and A. Ueda, *J. Electrochem. Soc.*, 1994, **141**, 2972–2977.

27 M. Jeong, H. Kim, W. Lee, S. J. Ahn, E. Lee and W. S. Yoon, *J. Power Sources*, 2020, **474**, 228592.

28 H. Deng, I. Belharouak, Y. K. Sun and K. Amine, *J. Mater. Chem.*, 2009, **19**, 4510–4516.

29 W. Liu, P. Oh, X. Liu, M. J. Lee, W. Cho, S. Chae, Y. Kim and J. Cho, *Angew. Chem., Int. Ed.*, 2015, **54**, 4440–4457.

30 H. H. Ryu, K. J. Park, C. S. Yoon and Y. K. Sun, *Chem. Mater.*, 2018, **30**, 1155–1163.

31 L. Liang, X. Li, M. Su, L. Wang, J. Sun, Y. Liu, L. Hou and C. Yuan, *Angew. Chem., Int. Ed.*, 2023, **62**, e202216155.

32 X. D. Zhang, J. L. Shi, J. Y. Liang, Y. X. Yin, J. N. Zhang, X. Q. Yu and Y. G. Guo, *Adv. Mater.*, 2018, **30**, 1801751.

33 C. Hong, Q. Leng, J. Zhu, S. Zheng, H. He, Y. Li, R. Liu, J. Wana and Y. Yang, *J. Mater. Chem. A*, 2020, **8**, 8540.